Chemical Engineering Journal 431 (2022) 134036

Contents lists available at ScienceDirect

Chemical Engineering Journal

journal homepage: www.elsevier.com/locate/cej

Tailored interface stabilization of FTO transparent conducting electrodes boosting electron and Li ion transport for electrochromic energy-storage devices

Myeong-Hun Jo [a], Bon-Ryul Koo [b], Kue-Ho Kim [a], Hyo-Jin Ahn [a,b,*]

[a] Department of Materials Science and Engineering, Seoul National University of Science and Technology, Seoul 01811, South Korea
[b] Program of Materials Science & Engineering, Convergence Institute of Biomedical Engineering and Biomaterials, Seoul National University of Science and Technology, Seoul 01811, South Korea

ARTICLE INFO

Keywords:
Interface stabilization
Transparent conducting electrode
Charge transport behaviors
Ultra-fast switchability
Cycle stability
EC energy-storage devices

ABSTRACT

Transparent conducting electrodes (TCEs) play an important role in transporting electrons to an active layer, which directly affects electrochemical reactions in electrochromic (EC) energy-storage devices. However, homogeneous and fast electron supply to electrochemically active layer is mainly limited by interfacial properties of the TCE. Especially, a rough interfacial structure leads to redundant voids for electron scattering, and an oxygen vacancy acts as an intrinsic electron-trapping site in TCE. Thus, we propose a highly smooth morphology and oxygen vacancy passivated TCE to boost electron and Li ion transport without an active material (WO_3) adjustment. These nanostructures are synthesized with simultaneous effects of W co-doping and H_2O_2 during spray pyrolysis deposition (W-FTO/H_2O_2) for application in EC energy-storage devices. The highly dense and smooth surface of W-FTO/H_2O_2 provides a homogeneous electron supply to WO_3, which induces uniform Li ion transport into WO_3. And the oxygen vacancy passivated structure encourages electron mobility, which leads to in-depth Li ion transport. Consequently, the EC energy-storage electrodes fabricated with W-FTO/H_2O_2 as a TCE exhibited ultra-fast switching speeds (2.3 s for coloration and 0.6 s for bleaching) and a high rate capability because of the high electron mobility. An all-solid-state cell fabricated with W-FTO/H_2O_2 as a TCE exhibited remarkable cyclic stability (transmittance retention of 92% and specific capacitance retention of 95.8% after 2,000 continuous cycles) because of the homogeneous electron transfer at the interface. Therefore, we demonstrate that tailoring interface structure of TCE is a promising strategy to improve the performance of EC energy-storage devices.

1. Introduction

Extensive advances in electrochemical-reaction-based energy-saving applications, such as Li ion batteries, supercapacitors, fuel cells, and electrochromic (EC) devices, have been achieved over the last few decades [1–3]. Notably, EC devices, which can save ~ 40% of the total energy consumption of a building when used as smart windows, are considered promising for use in energy-saving applications to modulate external solar heat with reversible color changes [4]. EC devices have a sandwich structure with a sequence of layers that include a transparent conducting oxide, a cathodic layer, an electrolyte, an anodic layer, and a transparent conducting oxide. The color changes in EC devices are derived from the insertion/extraction of Li ions and electrons at the active layers (cathodic and anodic layers) during reduction/oxidation (redox) reactions [5]. Because the color change progress in EC devices is accompanied by the transport of Li ions and electrons, EC devices can simultaneously perform an energy-storage function similar to pseudocapacitors. Thus, the multi-functionality provided by color changes and energy storage broadens the application potential of EC devices to include EC energy-storage devices such as EC supercapacitors and EC batteries, which can indicate the level of stored energy and real-time energy consumption through their color variations [6,7]. Hence, function-integrated EC energy-storage devices are highly desirable for future applications. However, some significant shortcomings, such as cycle stability and switching kinetics, hinder the successful commercialization of EC energy-storage devices.

* Corresponding author.
E-mail address: hjahn@seoultech.ac.kr (H.-J. Ahn).

https://doi.org/10.1016/j.cej.2021.134036
Received 15 September 2021; Received in revised form 14 November 2021; Accepted 3 December 2021
Available online 9 December 2021

Because of the sandwich-layered configuration of EC energy-storage devices, developing their interfacial properties could be a powerful strategy to promote Li ion and electron transport such that the long cycle stability and switching kinetics of the devices are improved. To upgrade the long cycle stability, hybrid structures like core–shell and organic–inorganic active materials have been fabricated for reversible charge transport at the active layer/electrolyte interface during the electrochemical reaction [8,9]. Additionally, to enhance the switching kinetics, many research groups have synthesized porous and composite structures that increase the Li ion diffusivity and electron conductivity, respectively, of the active materials, which affect the electrochemical kinetics at the active layer/electrolyte interface [10,11]. Most past studies have mainly focused on adjusting the active materials to improve the electrochemical behavior at the active layer/electrolyte interface. However, as much as the active layer/electrolyte interfacial properties have been adjusted, the interfacial properties of the transparent conducting electrode (TCE) play an important role in supplying homogeneous and fast electron transport to the active layers, which directly affects the electrochemical reversibility and kinetics of EC energy-storage devices. Nevertheless, the introduction of a TCE with tailored interface properties, such as surface morphology and chemical bonding states of transparent conducting oxides to achieve exceptionally fast and stable EC energy-storage devices has not been performed.

When the TCE surface morphology in this connection is rough, redundant voids can be formed between the TCE and WO_3 layer, which is a representative cathodic EC material, after the spin-coating and annealing process. These voids function as barriers for the electron pathway into the WO_3 layer and the preferred delamination centers of WO_3 by repetitive electrochemical reactions [12,13]. Additionally, a rough interfacial structure for a TCE not only increases the electron scattering at the interface but also allows charge aggregation to develop, which enforces inhomogeneous electron transport, resulting in an inferior electrochemical reversibility [14]. At the same time, the introduced oxygen vacancy (V_O) acts as an intrinsic electron-trapping site in TCE, resulting in decreased electron mobility related to the electrochemical kinetics. Additionally, the interfacial V_O can provide Li ion trapping sites during electrochemical reactions, reducing the reversibility [15,16]. Therefore, inducing a TCE interface stabilized structure with a uniform morphology and low V_O concentration, leading to homogeneous and rapid charge transport, can be a fundamental method to improve the cyclic stability and switching kinetics of EC energy-storage devices.

In this study, a highly dense and smooth interfacial morphology and an oxygen vacancy passivated structure of fluorine-doped tin oxide (FTO) films were developed based on the simultaneous effects of W co-doping and H_2O_2 during ultrasonic spray pyrolysis deposition, which stabilizes the interface of the TCE for EC energy-storage devices. The highly dense and smooth interfacial morphology of FTO facilitates a homogeneous electron supply to the WO_3 layer, which results in reversible electrochemical reactions in EC energy-storage devices. Additionally, the oxygen vacancy passivated structure of FTO enables rapid electron transport to WO_3, leading to ultra-fast electrochemical kinetics. We believe that the interface stabilized FTO is impactful as a TCE, giving rise to homogeneous and fast charge transport, and can be a novel solution to enhance the cycle stability and switching kinetics of EC energy-storage devices.

2. Materials and methods

Three types of FTO films were fabricated using ultrasonic spray pyrolysis deposition (USPD). The precursor solution for the bare FTO films was prepared by dissolving 0.68 M of tin chloride pentahydrate ($SnCl_4{\cdot}5H_2O$, SAMCHUN) and 1.20 M of ammonium fluoride (NH_4F, JUNSEI) in deionized (DI) water with 5 vol% ethyl alcohol (C_2H_5OH, Duksan). To obtain the W co-doped FTO films (W-FTO), 2 at% tungsten chloride (WCl_6, Aldrich) was added to the bare FTO precursor solution. The tailored interface-stabilized FTO films were prepared by adding 13.5 vol% hydrogen peroxide (H_2O_2, JUNSEI) to the W-FTO precursor solution (W-FTO/H_2O_2). The precursor solutions for the three types of FTO films were stirred for 4 h until they became transparent. Prior to the USPD, the glass substrate (Eagle XG^{TM}, Corning) was cleaned with ethanol and DI water to ensure the uniform deposition of the FTO films. All the precursor solutions were ultrasonic spray pyrolysis deposited on the glass substrates rotating at 5 rpm in a furnace maintained at 420 ℃ by using an ultrasonic atomizer (1.6 MHz). The flow rates of the carrier gas (air composed of 78% N_2 and 21% O_2) and deposition times of all the FTO films were the same at 15 L/min and 23 min, respectively. In addition to the synthesized FTO films, commercial FTO films (7.7 Ω/□) were purchased from Pilkington and used after cleaning with ethanol and DI water.

Thereafter, a WO_3 film (effective area of 3.4 cm^2) was equally spin-coated on the three types of fabricated FTO films (bare FTO, W-FTO, and W-FTO/H_2O_2) and commercial FTO for application to EC energy-storage devices. The precursor solution for the WO_3 films was prepared by dissolving 10 wt% tungsten chloride (WCl_6, Aldrich) in 2-propanol ($(CH_3)_2CHOH$, Aldrich) for 3 h while stirring in a glove box maintained with an Ar atmosphere. The obtained transparent blue WCl_6 solution was spin-coated twice on the FTO films at 2,000 rpm for 30 s, and then the spin-coated WCl_6 films were annealed at 300 ℃ for 1 h, resulting in WO_3. Therefore, four types of EC energy-storage electrodes, composed of WO_3 coated FTO films on a glass substrate (namely, WO_3//bare FTO, WO_3//W-FTO, WO_3//W-FTO/H_2O_2, and WO_3//commercial FTO) were successfully obtained.

The surface morphology and topography of each FTO film were characterized using field emission scanning electron microscopy (FESEM; Hitachi S-4800) and atomic force microscopy (AFM; PSIA XE-100). The crystal structure of each FTO film was investigated using X-ray diffraction (Rigaku D/max 2500, Cu K_α radiation). To reveal the chemical bonding states of the FTO films, X-ray photoelectron spectroscopy (XPS; ESCALAB, Cu K_α radiation) and Fourier transform infrared spectroscopy (FTIR; Thermo Fisher Scientific, Nicolet-iS50) were performed. The electrical and optical properties of the FTO films were measured using a Hall-effect measurement system (Ecopia, HMS-3000) and ultraviolet–visible (UV–vis) spectroscopy (Perkim-Elmer, Lambda-35), respectively.

The electrochemical and EC energy-storage performances of all the FTO films as TCEs were established using a three-electrode system consisting of WO_3 coated FTO half-cells as the working electrode, Ag wire as the reference electrode, and Pt wire as the counter electrode with 1 M of $LiClO_4$ (in propylene carbonate) as the electrolyte. To investigate the *in-situ* EC energy-storage performance, UV–vis spectroscopy and potentiostat/glavanostat (Metrohm Autolab, PGSTAT302N) measurements were used in simultaneous collaboration. For the electrochemical impedance spectroscopy (EIS), a potentiostat/galvanostat was utilized by using a sinusoidal signal with a 10 mV amplitude in the frequency range of 0.1–100 kHz. To obtain three-dimensional (3D) images and depth profiles for the Li ion behaviors, time-of-flight secondary ion mass spectroscopy (ToF-SIMS; ION-TOF, Korea Institute of Science and Technology) analyses were conducted.

To fabricate all-solid-state cells for EC energy-storage devices, each component was successfully united with the WO_3 coated FTO substrate (effective area of 3.4 cm^2) as the working electrode (WO_3//bare FTO, WO_3//W-FTO, WO_3//W-FTO/H_2O_2, and WO_3//commercial FTO), a Pt coated glass substrate as the counter electrode, and a gel polymer electrolyte. The precursor solution for the Pt films was prepared by dissolving 4 M chloroplatinic acid hydrate ($H_2PtCl_6{\cdot}6H_2O$, Aldrich) in 2-propanol ($(CH_3)_2CHOH$, Aldrich). After stirring for 3 h, the transparent yellow solution was spin-coated once on the glass substrate at a speed of 2,000 rpm for 30 s, then the films were annealed at 450 ℃ for 30 min in a box furnace, resulting in Pt counter electrode. To prepare the gel polymer electrolyte, 2.5 M lithium perchlorate ($LiClO_4$, Aldrich) was dissolved in the solvent that is composed of propylene carbonate ($C_4H_6O_3$, Aldrich) and acetonitrile (C_2H_3N, Aldrich). After stirring for 1

min, 10 wt% poly(methyl methacrylate) (PMMA, Aldrich) was added, and then the solution was stirred in a chemical bath at 50 ℃ for 1 h. Finally, the transparent solution was dried in the oven at 110 ℃ for 8 h, resulting in the gel polymer electrolyte. The working and counter electrodes were assembled together with gel polymer electrolyte by double layered tape (3 M, 60 μm thickness per layer) as a spacer frame, then the assembled electrodes were dried in a vacuum oven at 50 ℃ for 6 h, resulting in the all-solid-state cells.

3. Results and discussion

Fig. 1 shows schematic representation of preparation process of a working electrode and a counter electrode, and corresponding assembly of all-solid-state devices for three types of FTO films as a TCE (bare FTO, W-FTO, and W-FTO/H_2O_2). Three types of FTO films were successfully synthesized with different kinds of precursor solutions via USPD. Significantly, to realize identical properties of WO_3 films, we conducted a spin-coating and an annealing process under the same atmosphere in an enclosed chamber. As a result, we could obtain a consistent thickness in the range of ~ 198.93–211.03 nm and homogeneous morphology of WO_3 layers on all FTO films as shown in top-view and cross-sectional FESEM images (Figure S1).

Modifying the surface morphology of the FTO films for the TCE is suggested as a fundamental method to promote the electrochemical behaviors of electrons and Li ions by designing interfaces with the active WO_3 material for EC energy-storage devices. Fig. 2(a–f) show top-view and cross-sectional FESEM images of the (a and d) bare FTO, (b and e) W-FTO, and (c and f) W-FTO/H_2O_2 films. The surfaces of all FTO films were interlocked with pyramid-shaped crystallites. For a surface morphology comparison, Fig. 2(a and b) show that W-FTO exhibited an increased ratio of small-sized crystallites among the larger crystallites, as compared to bare FTO, generating relatively a compact surface structure. This was generated by the W-doping effect, which creates additional nucleation sites at the grain boundaries, leading to heterogeneous nucleation [17,18]. Consistent with the surface morphology, the crystallite size distribution of W-FTO exhibited two different Gaussian-fitted size scales, with small-sized crystallites (~144.9–184.6 nm) found among larger ones (~312.6–371.2 nm), leading to a compact structure, whereas bare FTO exhibited only one size scale (~280.3–384.2 nm) (Figure S2). In addition, the cross-sectional SEM images in Fig. 2(d and e) show that W-FTO exhibited a slightly lower surface roughness, as compared to bare FTO. As shown in AFM results in Figure S3, the root-mean-square roughness (R_{ms}) of W-FTO slightly declined to 31.46 nm from that of bare FTO (35.19 nm). The reduced surface roughness of W-FTO is theorized to be due to the suppressed (1 1 0) orientation corresponding to the pyramidal shape of the crystallites. This can be explained by the increase in HCl gases generated from the pyrolysis of WCl_6 adsorbing on polar flat (F)-faces {1 0 1}, thus slowing the (1 1 0) growth, which is also supported by the XRD results in Fig. 2g [19]. In contrast, the kurtosis roughness (R_{ku}) values, which indicate the roughness distribution uniformity, were similar between the bare FTO (2.89) and W-FTO (2.90), as confirmed by AFM (Figure S3). If $R_{ku} < 3$, a sample has a widespread roughness range, while $R_{ku} > 3$ indicates a narrow roughness range [20]. A surface morphology with heterogeneous roughness (low R_{ku}) restrained the electron transport by disturbing homogeneous electron transport and creating voids at the interface between the FTO and WO_3 layer. These generated voids not only act as electron scattering centers, but also generate the preferred delamination of a WO_3 layer with long-repetitive electrochemical reactions. Accordingly, W-FTO, which exhibited a heterogeneous roughness, would be inappropriate as a TCE for EC energy-storage devices with a long life. The W-FTO/H_2O_2, which exhibited a reduced R_{ms} and high R_{ku}, maintained an interface stabilized morphology to provide a homogeneous electron supply to the repeated electrochemical reactions. In Fig. 2(c and f), W-FTO/H_2O_2 shows a densely packed morphology and a smooth surface. Accordingly, W-FTO/H_2O_2 displayed an extremely narrow crystallite size distribution in the range of ~ 165.8–198.6 nm to sustain homogeneous grain growth (Figure S2). These interesting morphological changes could be explained by the crystallite growth behavior being influenced by the polarity of the planes. Generally, crystal growth of FTO films is heterogeneous, resulting in polycrystalline structure for the (1 1 0), (1 0 1), (2 0 0), and (2 1 1) planes [21]. Accordingly, many attempts have been made to characterize the (2 0 0) preferred orientation, which is related to

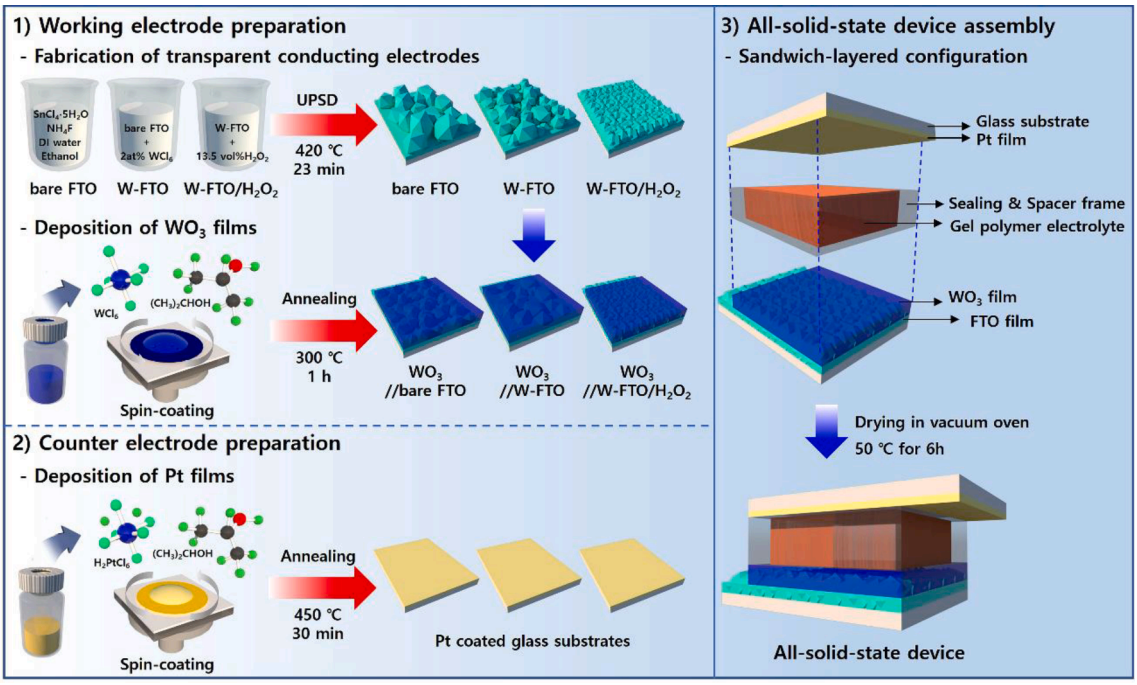

Fig. 1. Schematic representation of preparation process of a working electrode and a counter electrode, and corresponding assembly of all-solid-state devices for three types of FTO films as a TCE (bare FTO, W-FTO, and W-FTO/H_2O_2).

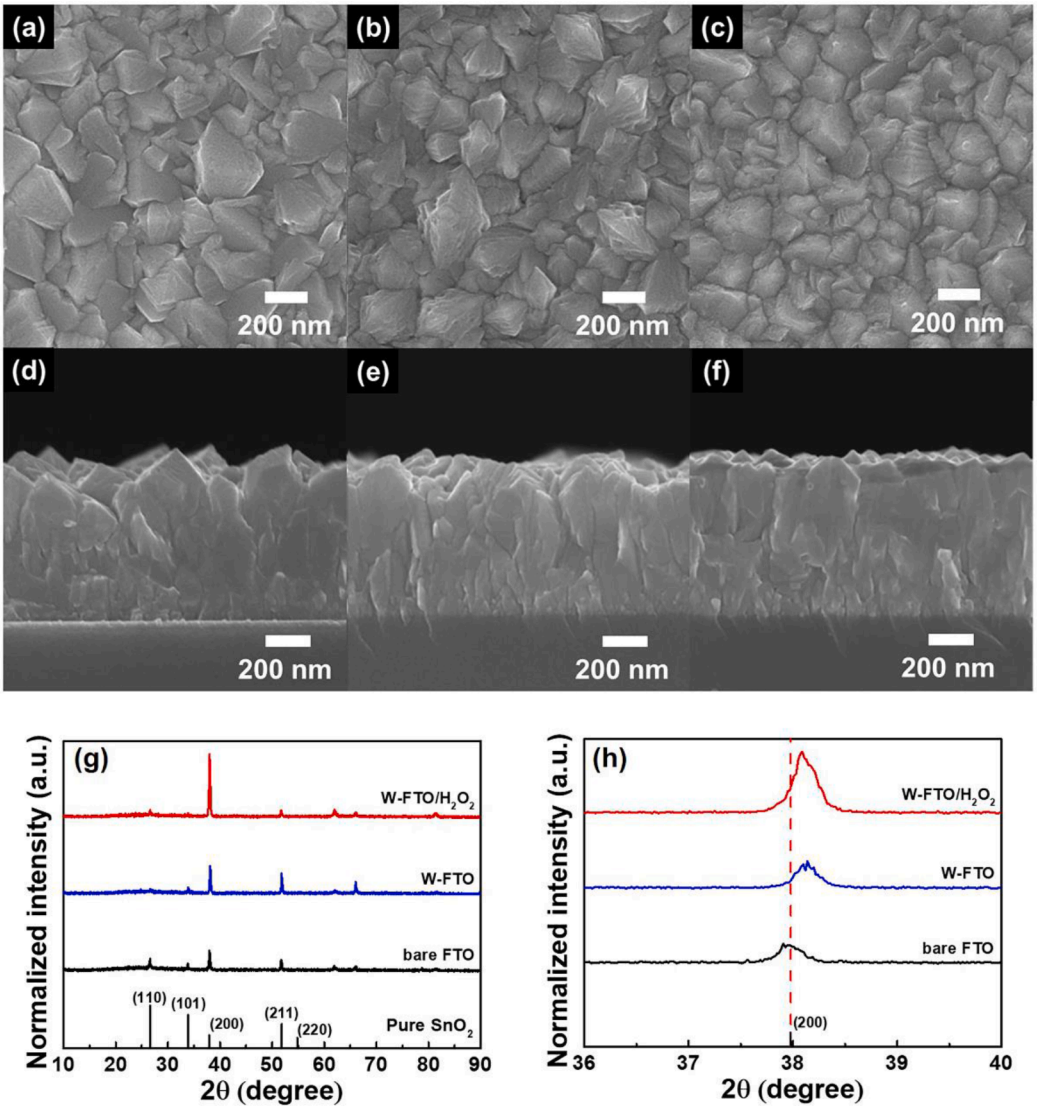

Fig. 2. Top-view and cross-section FESEM images of (a and d) bare FTO, (b and e) W-FTO, (c and f) W-FTO/H_2O_2, (g) XRD curves, and (h) enlarged XRD curves in the range of 36–40° of all FTO films.

a smooth surface and favored electron transfer channels, by increasing the polar halogen gases, such as HCl and HF, during pyrolytic deposition [22,23]. However, polycrystalline features and surface roughness limitations still exist due to the less-polar nature of exposed the (1 1 0), (1 0 1), and (2 1 1) planes, leading to the inferior adsorption of halogen gases. With the strong oxidizing property of H_2O_2, W-FTO/H_2O_2 retains an oxygen-rich bonded nature that can induce the polarity of the planes [24]. Thus, the plentiful HCl gases generated from WCl_6 and H_2O_2 can be vigorously adsorbed to the (1 1 0), (1 0 1), and (2 1 1) planes, which suppresses the crystal growth related to the pyramidal-shaped grains. Accordingly, W-FTO/H_2O_2 exhibited a high crystallinity in the strongly (2 0 0) preferred orientation with suppressed specific peaks, as confirmed in Fig. 2g. Therefore, the highly dense and smooth surface of W-FTO/H_2O_2 is expected to the result of the strong (2 0 0) preferred crystal growth being suppressing in different crystal growth directions. Because of the ability of H_2O_2 to produce a dense and smooth morphology, considerable roughness changes were observed in the AFM results (Figure S3). The W-FTO/H_2O_2 exhibited a narrow roughness distribution, consistent with the high R_{ku} value of 3.92, and an extremely reduced R_{ms} of 22.19 nm. We additionally observed a surface morphology of commercial FTO films to verify the interface stabilization of the W-FTO/H_2O_2. In Figure S4(a–c), the commercial FTO showed high and heterogeneous surface roughness with R_{ms} of 35.02 nm and R_{ku} of 3.16, which is far from the homogeneous carrier transport to an active layer. In this stream, the interfacial morphology of W-FTO/H_2O_2, which retains low R_{ms} and high R_{ku}, confirmed the interface stabilization of TCE, which supports homogeneous electron transfer at the interface of the WO_3 layer.

The crystal structure that accelerates the electron transfer of the FTO films was confirmed by XRD analysis (Fig. 2(g and h)). The three types of FTO films exhibited the crystalline structures with characteristic diffraction peaks that are well matched with the tetragonal rutile SnO_2 of (1 1 0), (1 0 1), (2 0 0), and (2 1 1) planes at 26.6°, 33.89°, 37.99°, and 51.82° (JCPDS no. 88–0287), respectively. Additionally, the enlarged XRD of the (2 0 0) plane in Fig. 2h shows that the bare FTO exhibited a slightly lower diffraction angle (37.93°) than that of pure SnO_2. This was a result of the substitution of O^{2-} (ionic radius of 0.132 nm) with the larger F^- (0.133 nm), which indicates successful FTO formation based on Bragg's law ($n\lambda = 2d\sin\theta$) [25]. However, the diffraction peaks of W-FTO and W-FTO/H_2O_2 shifted to a higher position than that of pure SnO_2. This is due to the substitution of Sn^{4+} (0.069 nm) with the smaller W^{6+} (0.060 nm), and is a proof of W-doping in FTO for both the W-FTO and W-FTO/H_2O_2 [26]. Furthermore, W-FTO exhibited an almost extinct (1 1 0) intensity, which is due to the WCl_6 producing HCl gases to

suppress the (1 1 0) growth, which was in good agreement with the reduced surface roughness and compact morphology of W-FTO. Accordingly, the W-FTO (2 0 0)/(1 1 0) ratio, which indicates the degree of parallel crystal growth, was enhanced, as compared to bare FTO (1.6), which is consistent with the reduced surface roughness. For W-FTO/H_2O_2, a drastically increased (2 0 0)/(1 1 0) ratio of 8.2, occurred as a result of the H_2O_2 effect, which supports the dense and smooth surface morphology.

XPS and FTIR analyses were performed to investigate the chemical bonding states of the three types of FTO films. In the Sn3d XPS results (Fig. 3a), $Sn3d_{2/5}$ and $Sn3d_{2/3}$ XPS core-level spectra of all the FTO films were separated into two characteristic peaks. One peak (blue filled) was located at approximately ~ 486.38 eV for $Sn3d_{5/2}$ and approximately ~ 494.80 eV for $Sn3d_{3/2}$, indicating a Sn-Sn bond, corresponding to the binding energy of Sn^{4+} in the SnO_2 phase. The other peak (red filled) was located at approximately ~ 487.31 eV for $Sn3d_{5/2}$ and ~ 495.73 eV for $Sn3d_{3/2}$ indicating a Sn-F chemical bond, which is a clear evidence of the F substitution in SnO_2 [25]. Thus, successful formation of F-doped SnO_2 phase can be determined from the Sn3d XPS results for all the samples. Additionally, to investigate the F doping concentration in the FTO films, the peak area ratio of Sn-F/Sn-Sn was calculated for all samples, as shown in red bars in Fig. 3c. The bare FTO and W-FTO exhibited similar F doping concentrations (0.286 for bare FTO and 0.282 for W-FTO). This indicates that W^{6+} substitution into Sn^{4+} was accomplished without a reduction in the F doping concentration in SnO_2 due to the lower electronegativity of W (1.47) compared to that of Sn (1.96), leading to an alleviated electron capture, which can be attributed to the enhanced electron density. Likewise, W-FTO/H_2O_2 retained similar F doping levels (0.280 for Sn-F/Sn-Sn). Fig. 3b shows that the FTO samples identically revealed three characteristic peaks related to V_O, Sn-OH, and Sn-O bonding states at ~ 532.4, ~531.48, and ~ 530.20 eV, respectively, in the O1s XPS core-level results [27]. Interestingly, each FTO film exhibited different V_O concentration. To precisely compare the V_O concentration for the three types of FTO films, the peak area ratio of V_O/Sn-O was calculated, as shown by green bars in Fig. 3c. An increased V_O concentration (0.15) was generated for W-FTO/H_2O_2, as compared to bare FTO (0.11). When W atoms are substituted for Sn sites, additional V_O are introduced at the nearest neighbor sites of the W atom to form the preferred configurations of electronic structures with lowest total energies in W-doped SnO_2, which demonstrates the increased V_O in W-FTO [28]. Thus, the increased V_O generates extra free electrons, which leads to enhanced electrical conductivity as a result of high electron concentrations. In contrast, defective W-FTO films with rich V_O can limit facile electron supply by increasing lattice disorder and providing charge trapping sites, which guides the unfavorable interfacial structure for fast electron transport to the active WO_3 layer. Accordingly, it should be noted that an almost extinct V_O structure was generated in W-FTO/H_2O_2, originates from the strong oxidizing effect of H_2O_2·H_2O_2 decomposes into HO_2^- by the reaction of $H_2O_2 + OH^- \rightarrow HO_2^- + H_2O$ in the solution, with the resultant HO_2^- inducing a strong oxidizing property. HO_2^- triggers V_O passivation by combining with dangling bonds at vacant oxygen sites. Finally, after the pyrolysis at 420 ℃, the resultant W-FTO/H_2O_2 film retained a stabilized V_O passivated structure. Additionally, the chemical bonding states of the FTO films were demonstrated by FTIR analysis (Fig. 3d). The infrared features were equally emitted at 455.89, 473.70, and 599.32 cm^{-1} for all samples, and were matched with the vibration mode of O-Sn-O, Sn-F, and Sn-O, respectively [28]. W-FTO shows the weakest O-Sn-O vibration mode, as compared to the bare FTO and W-FTO/H_2O_2. This was attributed to the increased V_O, which deform the O-Sn-O vibration mode by forming a V_O-Sn-O group and compression effect induced by repulsive force between Sn^{4+} and V_O [29]. Therefore, the obvious enhancement of the O-Sn-O and Sn-O vibration modes in W-FTO/H_2O_2 ensured a V_O passivated structure, which is consistent with the XPS results. This V_O passivated structure can effectively relax the lattice distortion, which directly affects the electron mobility. To confirm the lattice distortion of all FTO films, the Urbach energy (E_u) was calculated, which was determined by the degree of structural disorder and imperfection in the films (Figure S5). Typically, E_u increases with the generation of vacancy defects in crystalline films [30]. The greatly reduced E_u of W-FTO/H_2O_2

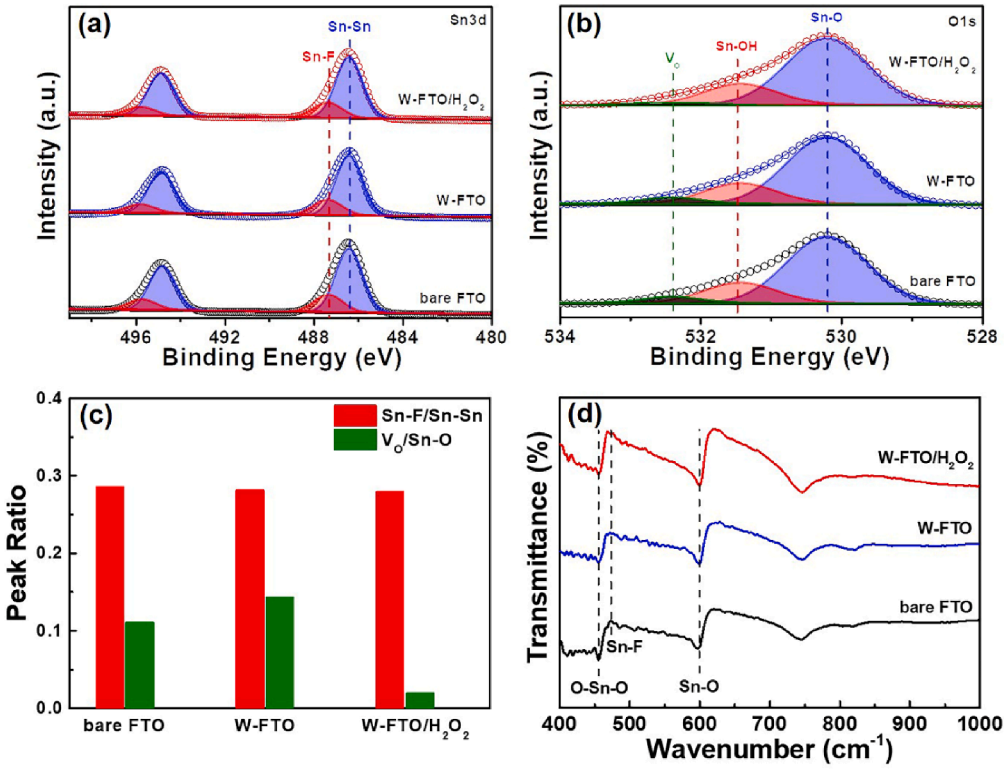

Fig. 3. XPS spectra of (a) Sn 3d and (b) O 1 s, (c) peak ratios of Sn-F/Sn-Sn and V_O/Sn-O, and (d) FTIR spectra obtained from all FTO films.

demonstrated the relaxed lattice distortion due to the V_O passivated structure. In contrast, W-FTO displayed an increased E_u. This was resulted from the abundant V_O, which could cause an inferior electron mobility. The XPS, FTIR, and E_u results shows excellent consistency, which contributes to the validity of the chemical bonding states for all FTO films. Therefore, W-FTO/H_2O_2 can induce the interface stabilization with V_O passivated structure, which boosts the electron mobility by relaxing lattice distortion and eliminating charge trapping sites at the interface.

The remarkable morphologies and chemical bonding states of W-FTO/H_2O_2 are expected to improve its electrical and optical properties, which have a direct impact on the EC energy-storage performances. Fig. 4a depicts the electrical properties of the three types of FTO films, including resistivity, carrier concentration, and Hall mobility. The carrier concentration drastically increased from bare FTO to W-FTO. This can be explained by the W-doping effect, which is the defect formation reaction of $W_{Sn}^{\bullet\bullet} + 2e^- + O_O + V_O^{\bullet\bullet} + 2e^- + 1/2O_2 \rightarrow SnO_2$:W. According to this reaction, W substitution generates four extra electrons with the simultaneous effects of high-valency W ions (W^{6+}) and V_O formation. Although, W-FTO/H_2O_2 showed a decreasing electron concentration tendency, as compared to W-FTO, it still retained a notable value of 8.47×10^{20} cm^{-3}. This carrier concentration behavior results from the decline in V_O due to the passivation effect of H_2O_2, while W substitution still provides two additional electrons. W-FTO displayed a lower Hall mobility value than bare FTO, which can be result from distorted lattice structure induced by the abundant V_O. Interestingly, W-FTO/H_2O_2 exhibited dramatic enhancement in Hall mobility, with a value of 31.17 $cm^2/(V\ s)$, as summarized in Table 1. The high Hall mobility of W-FTO/H_2O_2 is caused by the stabilized V_O passivated structure, which relaxes the lattice distortion and the electron trapping. As a result, because of the enhanced electron concentration by W co-doping and electron mobility by V_O passivation, W-FTO/H_2O_2 revealed an excellent electrical resistivity of 2.10×10^{-4} Ω·cm and a sheet resistance of 4.1 Ω/□. Fig. 4b shows optical properties of all the FTO films depicted as transmittance changes in the range of 300–900 nm. W-FTO/H_2O_2 exhibited a noticeable enhancement in transmittance in the full wavelength range, which shows a good visible transparency of 86.7%, as calculated by average transmittance at 400–700 nm. This was mainly attributed to the smooth surface morphology and reduced V_O to relieve the photon scatterings. On the other hand, commercial FTO showed inferior optical and electrical properties in comparison with W-FTO and W-FTO/H_2O_2, which supports the superior quality of the fabricated FTO films as a TCE (Figure S6). Consequently, when calculating the figure of merit, which represents the TCE quality of the electrical and optical properties, by using equation $\varphi = T^{10}/R_{sh}$, W-FTO/H_2O_2 showed the highest value of 5.58×10^{-2} Ω^{-1}, as compared to bare FTO and W-FTO (Figure S7a). Significantly, W-FTO/H_2O_2 showed the best TCE properties with an average transmittance of 86.7% and a sheet resistance of 4.1 Ω/□, as compared with previously reported FTO films (Figure S7(b and c)) [31–39]. Although the reported FTO films mainly focus on the dense morphologies with large grain size and low R_{ms}, W-FTO/H_2O_2 can hold the superior average transmittance and sheet resistance simultaneously, which results from the highly dense and smooth morphologies (low R_{ms} and high R_{ku}) and oxygen vacancy passivated structure, respectively, which is expected to enhance the electrochemical reactions of the EC energy-storage devices.

Table 1
Summary of electrical and optical properties of all FTO films.

	bare FTO	W-FTO	W-FTO/H_2O_2
Carrier concentration (cm^{-3})	5.73×10^{20}	9.90×10^{20}	8.47×10^{20}
Hall mobility ($cm^2/(V\ s)$)	26.24	24.34	31.17
Resistivity (Ω cm)	4.40×10^{-4}	2.49×10^{-4}	2.10×10^{-4}
Sheet resistance (Ω/□)	8.0	4.4	4.1
Transmittance (%)	80.3	80.0	86.7
Figure of merit ($\times 10^{-2}\Omega^{-1}$)	1.39	2.50	5.58

Fig. 5 shows the EC energy-storage performances of half-cells fabricated with each FTO as a TCE. All half-cells were equally coated with WO_3 under the same conditions throughout the spin-coating and annealing process to investigate the impacts of FTO on the EC energy-storage performances. Fig. 5a shows cyclic voltammetry (CV) curves measured using three electrode system from − 0.7 to 1.0 V (vs. Ag wire) at a scan rate of 20 mV/s. All samples displayed a broad redox curve without any sharp peaks, which is representative of the electrochemical behavior of amorphous WO_3 [40]. The amorphous WO_3 holds reversible color change by the insertion/extraction of Li ions and electrons under the applied voltage, as described by following equation (1):

$$WO_3(\text{bleached}) + xLi^+ + xe^- \leftrightarrow Li_xWO_3(\text{colored})$$

It should be noted that the CV area exhibited an increasing behavior from bare FTO to W-FTO/H_2O_2, which indicates enhanced electrochemical activity induced by the increased quantity of charge transports. A comparison of the bare FTO and W-FTO shows that the high electron concentration of W-FTO with lower sheet resistance triggers more activated electrochemical reactions in WO_3. Moreover, W-FTO/H_2O_2 showed a significant increase in the CV area. This indicates the outstanding reaction charge capacity of WO_3, which is influenced by the TCE property. The dense and smooth morphology of W-FTO/H_2O_2, devoid any protruding surface roughness, facilitated homogeneous electron transport throughout the WO_3 layer interface, which provokes the increased electrochemical redox reaction. The interfacial charge transfer resistance can be clearly demonstrated by analyzing EIS results in Figure S8. The series resistance (R_s), which is determined by the interfacial resistance between the TCE and active layer, showed the lowest value in W-FTO/H_2O_2, as compared to the other samples, which demonstrates the activated charge conductance. Furthermore, the

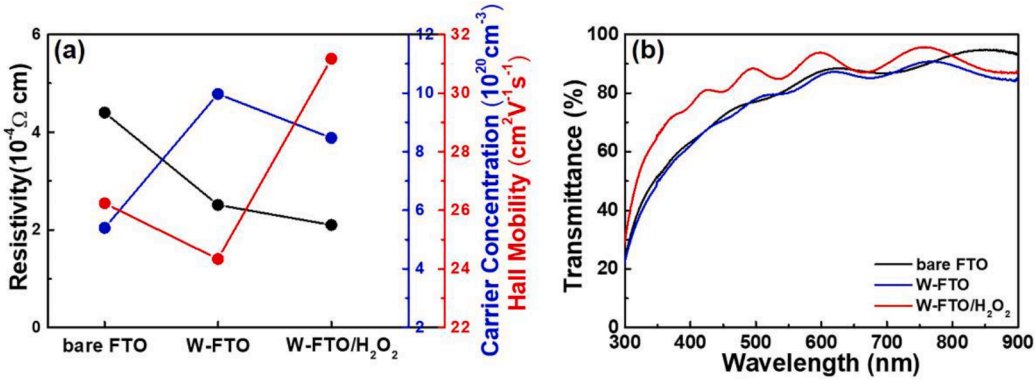

Fig. 4. Electrical and optical properties of all FTO films: (a) plots representing electrical properties of resistivity, carrier concentration, and Hall mobility, (b) transmittance variations in the wavelength range of 300–900 nm.

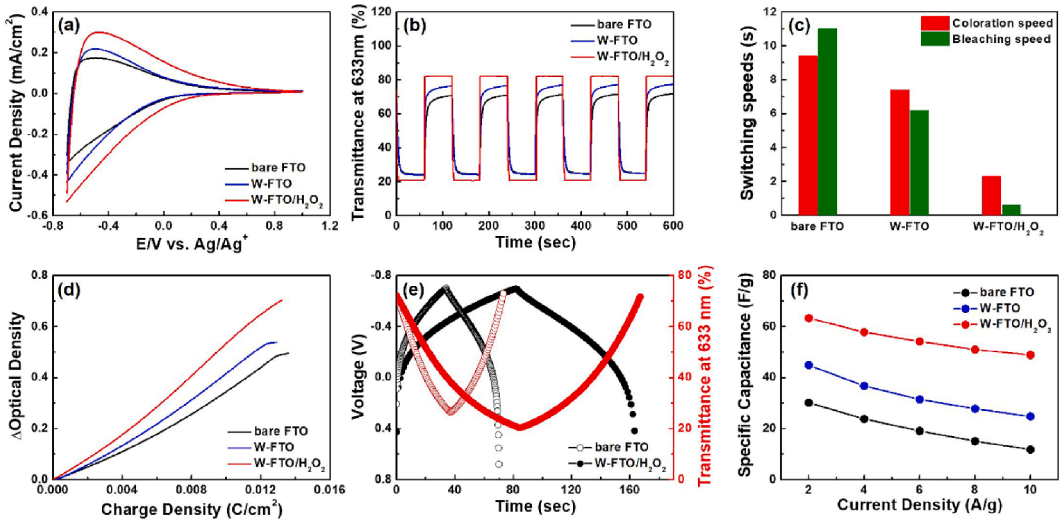

Fig. 5. Half-cell EC energy-storage performances fabricated by each FTO TCEs: (a) CV curves measured from –0.7 V to 0.3 V at a scan rate of 20 mV/s, (b) *In-situ* optical transmittances variations at –0.7 V for colored state and 0.3 V for bleached state for 60 s per process, (c) comparison of switching speeds among three types of FTO electrodes (WO_3//bare FTO, WO_3//W-FTO, and WO_3//W-FTO/H_2O_2), (d) optical density variations at 633 nm in response to inserted charge density, (e) galvanostatic charge/discharge curves at 1 A/g and following *in-situ* transmittance variations at 633 nm, (f) plots of specific capacitances with regard to 2–10 A/g.

Nyquist plot slope in the low-frequency region implies an ionic diffusion behavior, which is called the Warburg impedance [41]. The fact that W-FTO/H_2O_2 had the steepest slope in Warburg impedance showed that the electrode displayed the best Li ion diffusion kinetics. This result may be attributed to the oxygen vacancy passivated structure, which accelerates the fast electron transport to WO_3 layer, promoting the electrochemical kinetics. Figure S9 clearly shows Li ion diffusion behaviors with respect to the electrochemical kinetics. Figure S9(a – c) exhibited the CV curves of all electrodes, taken at gradually increased scan rates, retained their original profiles. Interestingly, a remarkable current density increase at both reduction and oxidation peaks was observed in W-FTO/H_2O_2, which could be identified from plots of peak current density against the scan rates for all electrodes under cathodic (triangles) and anodic (circles) reactions at – 0.4 V (Figure S9d). The Randles – Sevcik equation was used to calculate the Li ion diffusion coefficient (D_{Li}) using the results shown in Figure S9d [5]. The D_{Li} values shows an increasing tendency from bare FTO to W-FTO/H_2O_2 for both anodic and cathodic reactions, demonstrating the fast Li ion extraction and insertion (Figure S9e). The EC performances (Fig. 5b) showed excellent consistency with the electrochemical activity and kinetics for all electrodes. The *in-situ* transmittance curves at 633 nm were obtained by double-step chronoamperometry measurements under repeated potential variations of – 0.7 V (colored) and 1.0 V (bleached) for 60 s each, and the results are summarized in Table 2. Consistent with the electrochemical activity and kinetics, which are influenced by the electrical conductivity of TCE, W-FTO displayed an increased transmittance modulation ($\triangle T$) and fast switching speeds compared to the bare FTO. Interestingly, W-FTO/H_2O_2 displayed a rectangular transmittance curve and widened $\triangle T$ (61.2%), which are related to the ultra-fast and active EC performances, respectively. Also, the current density-time response of W-FTO/H_2O_2 displayed higher current density peaks and rapid response times for each redox potential, which shows great consistency with the enhanced $\triangle T$ and switching speeds, respectively. (Figure S10). Especially, with the novel influence of the oxygen vacancy passivated structure to accelerate the electron mobility, W-FTO/H_2O_2 exhibited the best switching speeds (2.3 s for coloration and 0.6 s for bleaching) among the three types of WO_3//FTO electrodes (Fig. 5c and Table 2). Additionally, W-FTO/H_2O_2 showed the highest coloration efficiency (CE), which is considered a crucial parameter for comprehensive verification of EC devices (Fig. 5d). The CE can be evaluated according to the change in optical density (OD) with the applied charge density (Q/A) as described in equations (2) and (3):

$$CE = \Delta OD/(Q/A) \tag{2}$$

$$\Delta OD = log(T_b/T_c) \tag{3}$$

The increase in CE is attributed to the transmittance modulation and switching speeds, which are influenced by the electrochemical activity and kinetics, respectively [7].

Fig. 5e shows the galvanostatic charge–discharge (GCD) curves (black line) at a current density of 1 A/g and the simultaneous transmittance variation (red line), which provides a pseudocapacitive ability to the EC electrodes. W-FTO/H_2O_2 showed a perfectly symmetric triangular GCD curve, indicating excellent electrochemical reversibility during charge–discharge, which originates from the enhanced electrochemical kinetics [42]. Additionally, the longer charge–discharge times of W-FTO/H_2O_2 indicates a higher energy storing capacity, showing good consistency with the enlarged $\triangle T$. Accordingly, W-FTO/H_2O_2 exhibited a better energy-storage capacity of 63.3F/g at 2 A/g as shown in Fig. 5f. In particular, W-FTO/H_2O_2 exhibited a superior high rate capability with a specific capacitance retention of 77.2 % at stepwise current densities from 2 – 10 A/g, which is directly affected by the high electron mobility. To prove a superiority of W-FTO/H_2O_2 as a TCE for EC energy-storage electrodes, we tested half-cell EC energy storage performances of commercial FTO as a TCE (Figure S11). As summarized in Table S1, the WO_3//commercial FTO exhibited inferior EC (lower transmittance modulation, switching speeds, and CE) and energy-storage performances (lower specific capacitance and high rate

Table 2
EC energy-storage performances of bare FTO, W-FTO, and W-FTO/H_2O_2 electrodes.

	Transmittance modulation (%, 633 nm)	Coloration speed (s)	Bleaching speed (s)	CE (cm^2/C)	Specific capacitance (F/g, at 2 A/g)
bare FTO	46.5	9.4	11.0	30.9	30.1
W-FTO	52.4	7.4	6.2	43.1	44.8
W-FTO/H_2O_2	61.2	2.3	0.6	52.9	63.3

capability). Thus, we suggest a TCE for high-performance EC electrodes could be fabricated by designing a stabilized interface to encourage the ultra-fast and electrochemical activity.

To investigate the feasibility of using such a device for both EC and energy-storage applications, all-solid-state cells consisting of WO_3 coated bare FTO, W-FTO, W-FTO/H_2O_2, and commercial FTO as the working electrode, Pt coated glass substrate as the counter electrode, and a gel polymer electrolyte ($LiClO_4$ + PMMA + PC) were fabricated. Fig. 6a shows transmittance variation across the wavelength range in a fully discharged state (2.0 V) and charged state (−2.0 V) of the multi-functional devices. As shown in Figure S12, W-FTO/H_2O_2 showed excellent transparency (83.8%) in the discharged state and deep blue color (32.3%) in the charged state, which demonstrates the successful operation of EC energy-storage devices. Accordingly, W-FTO/H_2O_2 exhibited a widened transmittance modulation of 51.5% at 633 nm than bare FTO (41.3%) and W-FTO (43.0%). Specially, the device fabricated with W-FTO/H_2O_2 as a TCE displayed outstanding long cycle stability in both EC and energy-storage function even after 2,000 continuous cycles with a transmittance retention ($\Delta T/\Delta T_o$) of 92.0% and a specific capacitance retention ($\Delta\eta/\Delta\eta_o$) of 95.8% while bare FTO and W-FTO shows drastic degradation from 500 cycles resulting in inferior cycle retention (Fig. 6(b and c)). Figure S13(a − c) shows transmittance variations at 633 nm over 2,000 cycles and Figure S13(g − i) shows GCD curves at 5th and 2,000th cycle of the three types of devices. W-FTO/H_2O_2 retains great transmittance modulation (46.35%) and specific capacitance (43.2F/g at 2A/g) after the 2,000 continuous cycles, compared to bare FTO (30.48% and 20.4F/g) and W-FTO (32.08% and 33.6F/g), which is attributed to the great electrochemical stability. From the transmittance variation curves within the middle of long cyclic EC measurement for three types of devices (Figure S13(d − f)), W-FTO/H_2O_2 revealed ultra-fast switching speeds (0.9 s for coloration and 0.7 s for bleaching) as a result of oxygen vacancy passivation effects, which accelerates the electron transport to an WO_3. Moreover, the EC energy-storage devices fabricated with W-FTO/H_2O_2 as a TCE showed improved CE (102.3 cm^2/C), which is mainly ascribed to the synergistic effect of the widened transmittance modulation and efficient charge transport (Figure S14). Additionally, the all-solid-state devices fabricated with W-FTO/H_2O_2 as a TCE displayed better optical memory performance, which is maintaining the colored states for much longer times under the open-circuit state (Figure S15). This can be attributed to the interface stabilization effects of TCE, which prevents the amount of internal electronic leakage in the electrodes. Consequently, all-solid-state device fabricated with W-FTO/H_2O_2 as a TCE exhibited the competitive specific capacitance and cyclic performances of specific capacitance retention, as compared to previously reported WO_3-based energy-storage devices [9,43–47] (Table S2). The EIS results after 5th and 2,000th cycles of W-FTO/H_2O_2 and bare FTO confirmed the electrochemical stability at the electrode/electrolyte interface (Figure S16). The bare FTO exhibited increased semi-circle radius, which indicates increased charge transfer resistance at the interface. This can be attributed to the poor electrochemical reversibility, which originates from the inferior electron transfer structure produced by the rough surface morphology and rich V_O structured FTO film. In contrast, W-FTO/H_2O_2 displayed a similar semi-circle radius after 2,000 cycles, indicating a thoroughly preserved charge transfer resistance at the interface. The tailored interface stabilization with a smooth surface and oxygen vacancy passivated structure of W-FTO/H_2O_2 induced homogeneous electron transport and fast electron mobility, respectively, leading to higher electrochemical activity and kinetics, which directly affects the electrochemical reversibility during long cycles. Additionally, to verify the superiority of the

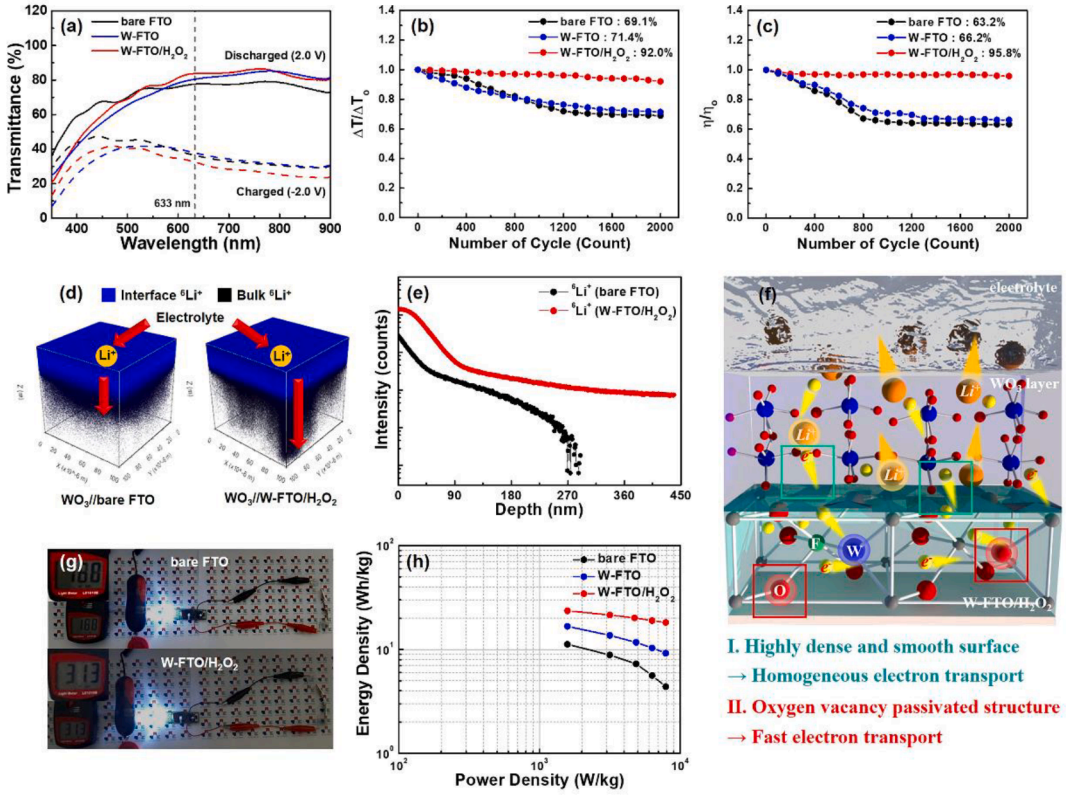

Fig. 6. All-solid-state EC energy-storage device performances fabricated by bare FTO and W-FTO/H_2O_2 TCEs: (a) transmittance variations in the wavelength range of 350–900 nm as result of discharged and charged state, (b) plots of transmittance retention ($\Delta T/\Delta T_o$) during 2,000 continuative coloration-bleaching, (c) plots of specific capacitance retention ($\Delta_\eta/\Delta_{\eta o}$) during 2,000 continuative charging-discharging, (d) 3D ToF-SIMS images of $^6Li^+$ distribution in the charged WO_3 layer, (e) $^6Li^+$ depth profiles of charged WO_3 layer, (f) schematic illustration of electrolyte//WO_3//W-FTO/H_2O_2 as a core route to promote Li ion and electron transports, (g) photograph of solid-state devices that are lighting the 1.5 V LED, (h) Ragone plots showing energy density vs. power density of three types of devices.

fabricated FTO films as a TCE for EC energy-storage devices, we tested EC energy-storage performances of all-solid-state cell that is composed of commercial FTO as a TCE. The all-solid-state EC energy-storage cell which is composed of commercial FTO as a TCE showed inferior long cycle stability of a transmittance retention (43.2%) and a specific capacitance retention (41.0%) after continuous 2,000 cycles (Figure S17). The commercial FTO revealed drastic degradation in both EC and energy-storage function from 100 cycles, which results from the rough surface morphology and low electron mobility of FTO. To demonstrate the behavior of Li ions in the electrode, ToF-SIMS analyses were performed on the bare FTO and W-FTO/H_2O_2 electrodes after charging for the same duration and under the voltage. Fig. 6d shows 3D images from ToF-SIMS depth profile experiments showing the spatial distribution of the elemental $^6Li^+$ in a space of 100 μm (x-axis) × 100 μm (y-axis) × 450 nm (z-axis, depth). The blue spots represent intercalated Li ions at the WO_3/electrolyte interface up to a depth of approximately ~ 150 nm, where both bare FTO and W-FTO/H_2O_2 exhibited similar distributions, meaning that uniform Li^+ intercalation was achieved near the interface, regardless of the TCE property. In contrast, black spots representing the in-depth Li ions in the bulk WO_3 film revealed different distribution states, as compared to bare FTO and W-FTO/H_2O_2. W-FTO/H_2O_2 exhibited an in-depth Li ion distribution along the z-axis towards the TCE, which was generated by the oxygen vacancy passivated structure, facilitating fast electron mobility. Fig. 6e shows the depth profiles of $^6Li^+$ for bare FTO and W-FTO/H_2O_2, as obtained from the 3D images. First, W-FTO/H_2O_2 presented slightly increased Li^+ quantity, as compared to bare FTO, which results from the decreased charge-transfer resistance to activate electrochemical activity as confirmed in EIS (Figure S8 and Figure S16). Additionally, W-FTO/H_2O_2 showed excellent Li^+ concentration maintenance to a depth of 450 nm, whereas bare FTO exhibited a sharp decline, leading to a relatively shallow Li ion intercalation. To provide clear evidence for homogeneous Li^+ intercalation over the entire area of the electrode, local Li^+ depth profiles for 10 randomly chosen points (100 × 100 nm^2) on the WO_3 surface, as shown in Figure S18, were investigated. W-FTO/H_2O_2 showed in-depth Li^+ profiles for all 10 points, as compared to bare FTO, supporting the uniform Li^+ intercalation throughout the WO_3 layer, which results from the homogeneous electron transport of the TCE. Fig. 6f depicts a schematic illustration of the tailored interface stabilization of W-FTO/H_2O_2 as a fundamental method to promote homogeneous and fast charge transport. For a more direct understanding of the multi-functionality of EC energy-storage devices, LED (FK185, 1.5 V) was operated with the devices (Fig. 6g). The charged (colored) device could light up the LED until it was completely discharged (gradually turned to colorless), which demonstrated the successful operation of the multi-functional device. W-FTO/H_2O_2 exhibited stronger illumination intensity of 313 lx, as compared to bare FTO of 188 lx, which is attributed to the higher energy density of the electrode. This was further confirmed by the Ragone plot shown in Fig. 6h. W-FTO/H_2O_2 revealed higher energy density (23.6 W h/kg) at a power density of 1577.6 W/kg, maintaining a high energy density retention with an increasing power density, as compared to bare FTO and W-FTO.

4. Conclusion

An interface stabilized FTO was developed as a TCE by engineering the interface with active WO_3 layers as a fundamental method to promote electronic and ionic transport in EC energy-storage devices. W-FTO/H_2O_2 was successfully fabricated using simultaneous effects of W co-doping and H_2O_2 during spray pyrolysis deposition of FTO. The dense and smooth surface morphology of FTO induced homogeneous electron transport to WO_3, leading to a uniform Li ion transport. Additionally, the oxygen vacancy passivated structure promoted fast electron mobility, triggering enhanced electrochemical kinetics. Consequently, the EC energy-storage devices fabricated with W-FTO/H_2O_2 as a TCE exhibited excellent EC energy-storage performances. Specifically, ultra-fast switching speeds (2.3 s for coloration and 0.6 s for bleaching) and superior long cycle stability up to 2,000 cycles both in electrochromic and energy-storage function with high retention of 92% and 95.8%, respectively. Thus, the novel interfacial engineering of TCE to boost electron and Li ion transport can offer new possibilities for ultra-fast and stable EC energy-storage devices.

Declaration of Competing Interest

The authors declare that they have no known competing financial interests or personal relationships that could have appeared to influence the work reported in this paper.

Acknowledgements

This research was supported by Basic Science Research Program through the National Research Foundation of Korea (NRF) funded by the Ministry of Education (NRF-2021R1A6A1A03039981), and National R&D Program through the National Research Foundation of Korea (NRF) funded by Ministry of Science and ICT (2021M3D1A2047047).

Appendix A. Supplementary data

Supplementary data to this article can be found online at https://doi.org/10.1016/j.cej.2021.134036.

References

[1] D.-Y. Shin, K.-W. Sung, H.-J. Ahn, Fluorine-doped carbon quantum dot interfacial layer on stockade-like etched copper foil for boosting Li-ion storage, Chem. Eng. J. 413 (2021), 127563.
[2] Y. Yang, Y. Zhao, C. Tang, L. Xu, D. Morgan, R. Liu, Role of macrophyte species in constructed wetland-microbial fuel cell for simultaneous wastewater treatment and bioenergy generation, Chem. Eng. J. 392 (2020), 123708.
[3] M.-H. Jo, B.-R. Koo, H.-J. Ahn, Defective impacts on amorphous WO_3•H_2O films using accelerated hydrolysis effects for flexible electrochromic energy-storage devices, Appl. Surf. Sci. 556 (2021), 149664.
[4] G. Cai, J. Chen, J. Xiong, A.-L.-S. Eh, J. Wang, M. Higuchi, P.S. Lee, Molecular Level Assembly for High-Performance Flexible Electrochromic Energy-Storage Devices, ACS Energy Lett. 5 (2020) 1159–1166.
[5] K. Zhou, H. Wang, J. Jiu, J. Liu, H. Yan, K. Suganuma, Polyaniline films with modified nanostructure for bifunctional flexible multicolor electrochromic and supercapacitor applications, Chem. Eng. J. 345 (2018) 290–299.
[6] B.-R. Koo, M.-H. Jo, H.-J. Ahn, Amorphous-quantized WO_3•H_2O films as novel flexible electrode for advanced electrochromic energy storage devices, Chem. Eng. J. 424 (2021), 130383.
[7] T.G. Yun, M. Park, D.-H. Kim, D. Kim, J.Y. Cheong, J.G. Bae, S.M. Han, I.-D. Kim, All-Transparent Stretchable Electrochromic Supercapacitor Wearable Patch Device, ACS Nano 13 (2019) 3141–3150.
[8] B.-R. Koo, K.-W. Sung, H.-J. Ahn, Boosting Ultrafast Lithium Storage Capability of Hierarchical Core/Shell Constructed Carbon Nanofiber/3D Interconnected Hybrid Network with Nanocarbon and FTO Nanoparticle Heterostructures, Adv. Funct. Mater. 30 (2020) 2001863.
[9] Q. Guo, X. Zhao, Z. Li, D. Wang, G. Nie, A novel solid-state electrochromic supercapacitor with high energy storage capacity and cycle stability based on poly (5-formylindole)/WO_3 honeycombed porous nanocomposites, Chem. Eng. J. 384 (2020), 123370.
[10] D.-Y. Shin, J.S. Lee, B.-R. Koo, H.-J. Ahn, Hierarchical hybrid nanostructure of 1T-tungsten disulfide quantum dots/multihollow capillary bundle-type mesoporous carbon for ultrafast and ultrastable lithium storage, Chem. Eng. J. 412 (2021), 128547.
[11] L. Zhao, X. Huang, G. Lin, W. Peng, J. Peng, J. Chao, L. Yi, X. Huang, C. Li, W. Liao, Structure engineering in hexagonal tungsten trioxide/oriented titanium dioxide nanorods arrays with high performances for multi-color electrochromic energy storage device applications, Chem. Eng. J. 420 (2021), 129871.
[12] L. Jablonka, L. Riekehr, Z. Zhang, S.-L. Zhang, T. Kubart, Highly conductive ultrathin Co films by high-power impulse magnetron sputtering, Appl. Phys. Lett. 112 (2018), 043103.
[13] Y. Li, Y. Qi, Energy landscape of the charge transfer reaction at the complex Li/SEI/electrolyte interface, Energy Environ. Sci. 12 (2019) 1286–1295.
[14] B.H. Kim, C.M. Staller, S.H. Cho, S. Heo, C.E. Garrison, J. Kim, D.J. Milliron, High Mobility in Nanocrystal-Based Transparent Conducting Oxide Thin Films, ACS Nano 12 (2018) 3200–3208.
[15] G.-C. Guo, R.-Z. Wang, B.-M. Ming, C. Wang, S.-W. Luo, C. Lai, M. Zhang, Trap effects on vacancy defect of C_3N as anode material in Li-ion battery, Appl. Surf. Sci. 475 (2019) 102–108.

[16] X. Zou, H.G. Ong, L. You, W. Chen, H. Ding, H. Funakubo, L. Chen, J. Wang, Charge trapping-detrapping induced resistive switching in $Ba_{0.7}Sr_{0.3}TiO_3$, AIP Adv. 2 (2012), 032166.
[17] S. Wang, J. Qin, Y. Zhang, F. Xia, M. Liu, H. Chen, M.A. Mamun, P. Liu, R. Rigway, G. Shi, J. Song, Y.L. Zhong, H. Zhao, Tungsten-doped nanocrystalline V_6O_{14} nanoparticles as low-cost and high-performance electrodes for energy storage devices, Energy Technol. 7 (2019) 1801041.
[18] N. Shen, B. Dong, C. Cao, Z. Chen, J. Liu, H. Luo, Y. Gao, Lowered phase transition temperature and excellent solar heat shielding properties of well-crystallized VO_2 by W doping, Phys. Chem. Chem. Phys. 18 (2016) 28010–28017.
[19] B.-R. Koo, D.-H. Oh, D.-H. Riu, H.-J. Ahn, Improvement of Transparent Conducting Performance on Oxygen-Activated Fluorine-Doped Tin Oxide Electrodes Formed by Horizontal Ultrasonic Spray Pyrolysis Deposition, ACS Appl. Mater. Interfaces 9 (2017) 44584–44592.
[20] M. Sedlacek, B. Podgornik, J. Vizintin, Correlation between standard roughness parameters skewness and kurtosis and tribological behaviour of contact surfaces, Tribol. Int. 48 (2012) 102–112.
[21] M. Calatayud, J. Andres, A. Beltran, A theoretical analysis of adsorption and dissociation of CH_3OH on the stoichiometric SnO_2 (110) surface, Surf. Sci. 430 (1999) 213–222.
[22] P. Karthick, K. Saravanakumar, C. Sanjeeviraja, K. Jeyadheepan, Realization of highly conducting and transparent SnO_2 thin films by optimizing F/Sn molar ratio for electrochemical applications, Thin Solid Films 713 (2020), 138362.
[23] L. Wang, J. Yu, X. Niu, L. Wang, C. Fu, R. Qiu, W. Yan, H. Zhao, J. Yang, Effect of F and Nb co-doping on structural, electrical and optical properties of spray deposited tin oxide thin films, Thin Solid Films 649 (2018) 147–153.
[24] A. Smith, J.-M. Laurent, D.S. Smith, J.-P. Bonnet, R.R. Clemente, Relation between solution chemistry and morphology of SnO_2-based thin films deposited by a pyrosol process, Thin Solid Films 266 (1995) 20–30.
[25] M.-H. Jo, B.-R. Koo, H.-J. Ahn, Accelerating F-doping in transparent conducting F-doped SnO_2 films for electrochromic energy storage devices, Ceram. Int. 46 (2020) 25066–25072.
[26] X. Wang, H. Ishiwara, Polarization enhancement and coercive field reduction in W- and Mo-doped $Bi_{3.35}La_{0.75}Ti_3O_{12}$ thin films, Appl. Phys. Lett. 82 (2003) 2479.
[27] X. Niu, W. Yan, C. Shao, H. Zhao, J. Yang, Hydrothermal synthesis of Mo-C co-doped TiO_2 and coupled with fluorine-doped tin oxide (FTO) for high-efficiency photodegradation of methylene blue and tetracycline: Effect of donor-acceptor passivated co-doping, Appl. Surf. Sci. 466 (2019) 882–892.
[28] B. Zhang, Y. Tian, J.X. Zhang, W. Cai, Fourier transformation infrared spectrum studies on the role of fluorine on SnO_2: F films, Appl. Phys. Lett. 98 (2011), 021906.
[29] B. Zhang, Y. Tian, J.X. Zhang, W. Cai, The role of oxygen vacancy in fluorine-doped SnO_2 films, Physica B 406 (2011) 1822–1826.
[30] P. Chetri, A. Choudhury, Investigation of optical properties of SnO_2 nanoparticles, Physica E 47 (2013) 257–263.
[31] B.-J. Li, Y.-Y. Wang, L.-J. Huang, H.-D. Cao, Q. Wang, H. Ding, N.-F. Ren, Influences of ultrasonic vibration on morphology and photoelectric properties of F-doped SnO_2 thin films during laser annealing, Appl. Surf. Sci. 458 (2018) 940–948.
[32] X.H. Shi, K.J. Xu, Properties of fluorine-doped tin oxide films prepared by an improved sol-gel process, Mater. Sci. Semicond. Process 58 (2017) 1–7.
[33] J. Kim, S. Wong, G. Kim, Y.-B. Park, J.V. Embden, E.D. Gaspera, Transparent electrodes based on spray coated fluorine-doped tin oxide with enhanced optical, electrical and mechanical properties, J. Mater. Chem. C 8 (2020) 14531–14539.
[34] B.-J. Li, G.-Y. Yang, L.-J. Huang, W. Zu, H. Li, Y.-L. Wang, S.-S. Li, N.-F. Ren, Surface morphology and photoelectric properties of FTO ceramic thin films under a simple transparent cover-assisted laser annealing, Mater. Res. Bull. 108 (2018) 151–155.
[35] L.T.C. Tuyen, S.-R. Jian, N.T. Tien, P.H. Le, Nanomechanical and Material Properties of Fluorine-Doped Tin Oxide Thin Films Prepared by Ultrasonic Spray Pyrolysis: Effects of F-Doping, Materials 12 (2019) 1665.
[36] M.J. Powell, D.B. Potter, R.L. Wilson, J.A. Darr, I.P. Parkin, C.J. Carmalt, Scaling aerosol assisted chemical vapour deposition: Exploring the relationship between growth rate and film properties, Mater. Des. 129 (2017) 116–124.
[37] K.D.A. Kumar, S. Valanarasu, K. Jeyadheepan, H.-S. Kim, D. Vikraman, Evaluation of the physical, optical, and electrical properties of SnO_2: F thin films prepared by nebulized spray pyrolysis for optoelectronics, J. Mater. Sci.-Mater. Electron. 29 (2018) 3648–3656.
[38] B.-J. Li, L.-J. Huang, N.-F. Ren, M. Zhou, Titanium dioxide-coated fluorine-doped tin oxide thin films for improving overall photoelectric property, Appl. Surf. Sci. 290 (2014) 80–85.
[39] J.-W. Bae, B.-R. Koo, H.-R. An, H.-J. Ahn, Surface modification of fluorine-doped tin oxide films using electrochemical etching for dye-sensitized solar cells, Ceram. Int. 41 (2015) 14668–14673.
[40] Y. Shi, Y. Zhang, K. Tang, J. Cui, X. Shu, Y. Wang, J. Liu, Y. Jiang, H.H. Tan, Y. Wu, Designed growth of WO_3/PEDOT core/shell hybrid nanorod arrays with modulated electrochromic properties, Chem. Eng. J. 355 (2019) 942–951.
[41] G.-H. An, J. Hong, S. Park, Y. Cho, S. Lee, B. Hou, S. Cha, 2D Metal Zn Nanostructure Electrodes for High-Performance Zn Ion Supercapacitors, Adv. Energy Mater. 10 (2020) 1902981.
[42] B.-R. Koo, K.-H. Kim, H.-J. Ahn, Novel tunneled phosphorus-doped WO_3 films achieved using ignited red phosphorus for stable and fast switching electrochromic performances, Nanoscale 11 (2019) 3318–3325.
[43] Q. Xu, Y. Yin, T. Gao, G. Cao, Q. Chen, C. Lan, F. Li, C. Li, Sputter deposition of Ag-induced WO_3 nanoisland films with enhanced electrochromic properties, J. Alloy. Compd. 829 (2020), 154431.
[44] J. Pan, R. Zheng, Y. Wang, X. Ye, Z. Wan, C. Jia, X. Weng, J. Xie, L. Deng, A high-performance electrochromic device assembled with hexagonal WO_3 and NiO/PB composite nanosheet electrodes towards energy storage smart window, Sol. Energy Mater. Sol. Cells 207 (2020), 110337.
[45] Y. Shi, M. Sun, Y. Zhang, J. Cui, W. Wang, X. Shu, Y. Qin, H.H. Tan, J. Liu, Y. Wu, Structure modulated amorphous/crystalline WO_3 nanoporous arrays with superior electrochromic energy storage performance, Sol. Energy Mater. Sol. Cells 212 (2020), 110579.
[46] W.-Q. Wang, X.-L. Wang, X.-H. Xia, Z.-J. Yao, Y. Zhong, J.-P. Tu, Enhanced electrochromic and energy storage performance in mesoporous WO_3 film and its application in a bi-functional smart window, Nanoscale 10 (2018) 8162.
[47] D. Zhou, F. Shi, D. Xie, D.H. Wang, X.H. Xia, X.L. Wang, C.D. Gu, J.P. Tu, Bi-functional Mo-doped WO_3 nanowire array electrochromism-plus electrochemical energy storage, J. Colloid Interface Sci. 465 (2016) 112–120.